Science Arts & Métiers (SAM)

is an open access repository that collects the work of Arts et Métiers Institute of Technology researchers and makes it freely available over the web where possible.

This is an author-deposited version published in: https://sam.ensam.eu
Handle ID: .http://hdl.handle.net/10985/17485

To cite this version :

Raphaël MOULART, Stéphane AVRIL, Fabrice PIERRON - Identification of the through-thickness rigidities of a thick laminated composite tube - Composites Part A: Applied Science and Manufacturing - Vol. 37, n°2, p.326-336 - 2006

Any correspondence concerning this service should be sent to the repository Administrator : scienceouverte@ensam.eu

Arts et Métiers Institute of Technology

Identification of the through-thickness rigidities of a thick laminated composite tube

Raphaël Moulart, Stéphane Avril*, Fabrice Pierron

Laboratoire de Mécanique et Procédés de Fabrication Ecole Nationale Supérieure d'Arts et Métiers, rue Saint-Dominique, BP 508, 51006 Cha^lons-en-Champagne Cedex, France

Abstract

In this paper, a novel experimental procedure is carried out for providing all the through-thickness rigidities of a thick glass-epoxy laminated ring cut from a tube, using only one diametral compression test. The procedure requires first to measure the strain field over a predefined area of the lateral surface of the ring coupon, and then to process it with the Virtual Fields Method. The region of interest where noise effects are minimized is first determined with simulated data. Then, the practical feasibility of the procedure is demonstrated with experimental data. The displacement fields are measured using the grid method. In order to filter the measurement noise at best, the strain fields are derived by polynomial fitting of the displacement fields. The validity of this approach is checked on simulated data. However, the experimentally identified stiffness values appear very scattered from one test to another. This is due to the non-uniform distribution of the load through the thickness, which is a well-known problem when testing thick composites. It has been shown that an optical system providing directly the images of both sides of the specimen can address this issue. Finally, such a system is set-up and successfully applied for identifying all the through-thickness rigidities of the ring.
© 2005 Elsevier Ltd. All rights reserved.

Keywords: B. Optical techniques; B. Anisoropy; D. Mechanical testing; Virtual fields method

1. Introduction

Composite materials structural components are usually based on thin plates or shells. In this case, only in-plane properties are required for design. However, composite applications tend now to spread out over industrial sectors such as the naval or ground transportation industry. These sectors require the use of less costly materials such as glass-reinforced polymers, for which increased thicknesses are necessary to fulfil the structural functions. For this type of applications, not only the in-plane but also the through-thickness properties are necessary.

The structure investigated in this paper is a filament-wound glass/epoxy composite tube used in off-shore applications for oceanographic electronic device encasing. The present study focuses on a ring coupon cut from the tube. Its thickness is 50 mm (Fig. 1) and its mean radius is 112.5 mm, meaning that the through-thickness mechanical behaviour significantly affects the response of the tube. The objective here is to identify its through-thickness rigidities.

Because of their relatively new development, the measurement techniques for the through-thickness rigidities of thick composites have seldom been studied up till now. Some of the available mechanical tests, which have been found in the literature, are:

- the tensile test on through-thickness waisted or non-waisted coupons [1,2],
- the Iosipescu shear test [3],
- the torsion test on a rectangular bar [1],
- a combined tensile and bending test on a curved coupon [4].

For all these tests, significant errors can occur if the boundary conditions provide unexpected gradients in the strain distribution. This requirement is difficult to fulfil for anisotropic materials because the anisotropy enhances

* Corresponding author.
E-mail address: stephane.avril@chalons.ensam.fr (S. Avril).

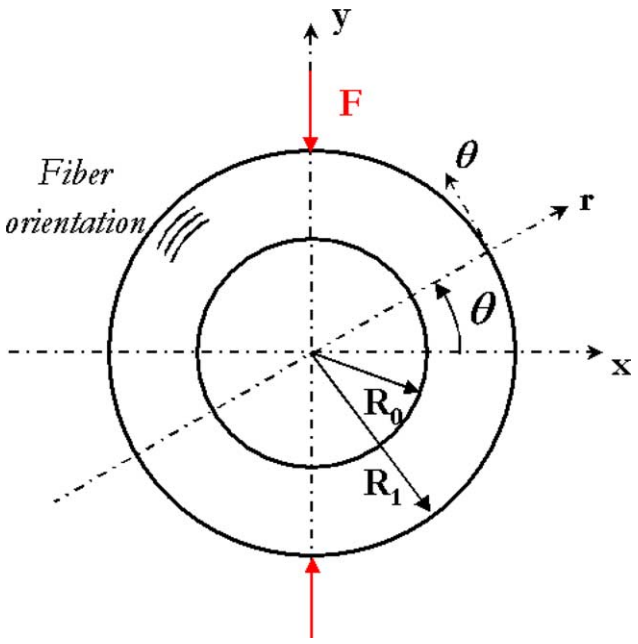

Fig. 1. Schematic of the ring compression test.

parasitic effects induced by imperfect boundary conditions [5,6]. Moreover, some specimens are difficult to prepare, like the waisted tensile specimen, and the strain gauging can be rather tiresome. Therefore, there is a great interest in developing novel experimental procedures suited to thick composites that will use coupons that are simple to prepare.

An alternative strategy to the above tests has been proposed in the literature a few years ago [7]. It requires the measurement of the full strain field over the surface of the specimen using an optical technique. The inverse problem can be solved with the Virtual Fields Method (VFM), which is based on the principle of virtual work. This approach is very promising since it can directly supply the whole set of parameters of the constitutive equations from the measurement of the heterogeneous strain fields over the whole or part of the specimen surface ([8–12], for instance). Contrary to finite element model updating [13], the VFM provides the unknown material parameters directly (in the case of elasticity at least) without the need of calibrating iteratively a finite element model of the test. Besides, it is rather insensitive to parasitic end-effects, which usually disturb the in-plane stress field, and no assumption is made on the displacement/strain/stress distributions. Only the form of the constitutive equations has to be assumed *a priori*.

The application of this approach to the identification of the through thickness rigidities of a thick laminated composite tube has already been the object of a feasibility study using simulated data [11]. It was shown that this diametral compression test gives rise to heterogeneous stress and strain fields in the specimen and that the use of suitable virtual fields enabled the simultaneous identification of all the material rigidities. However, no experimentation had been carried out. The aim of this study is to test experimentally the suitability of this approach for identifying the through thickness rigidities of the ring coupons.

After a numerical study devoted to the selection of the region of interest of the specimen, the practical feasibility of the procedure is shown with experimental data. Displacement fields are measured using the grid method and strain fields are derived by fitting displacement fields with polynomials. The obtained results appear very scattered. As this scatter is induced by non uniform load distribution through the depth of the ring, an improved procedure is finally developed for identifying more accurately the unknown stiffnesses by using back-to-back measurements.

2. The identification procedure

2.1. The diametral compression test

The sample tested here is a ring cut from a glass/epoxy composite tube. The ring symmetry is cylindrical and therefore, the polar coordinate system is chosen. The ring is studied in its transverse plane (r,θ). The fibres are in the θ-wise (i.e. circumferential) direction. (Fig. 1).

The ring dimensions are as follows: $R_0 = 87.5$ mm (inner radius), $R_1 = 137.5$ mm (outer radius) and $D = 21.5$ mm (depth of the coupon, the depth referring here to the dimension in the out of plane direction z).

It is assumed that the constitutive equations are linear elastic orthotropic.

The stress–strain relation is expanded using the convention of contracted indices ($rr \rightarrow R$, $\theta\theta \rightarrow \Theta$, $r\theta \rightarrow S$), which writes:

$$\begin{pmatrix} \sigma_R \\ \sigma_\Theta \\ \sigma_S \end{pmatrix} = \begin{bmatrix} Q_{RR} & Q_{R\Theta} & 0 \\ Q_{R\Theta} & Q_{\Theta\Theta} & 0 \\ 0 & 0 & Q_{SS} \end{bmatrix} \begin{pmatrix} \varepsilon_R \\ \varepsilon_\Theta \\ \varepsilon_S \end{pmatrix} \quad (1)$$

The different steps involved are as follows.

- The mechanical test:

It is a diametral compression test. It has been chosen because of its simplicity and its ability to generate a heterogeneous strain field inside the coupon [11].

- Full-field measurements:

The application of this procedure requires the measurement of the full strain field. Therefore, an optical full-field measurement technique is necessary. The grid method is used here [14,15].

- Identification:

The Virtual Fields Method is applied.

2.2. The Virtual Fields Method

The VFM has been introduced by Grédiac [7] and is based on the Principle of Virtual Work. According to this principle, at point M, the static global equilibrium of a coupon having a constant thickness D yields, for plane stress conditions and in absence of body forces:

$$D\int_S \underline{\underline{\sigma}} : \underline{\underline{\varepsilon}}^* \mathrm{d}S = \int_{S_f} \overrightarrow{T}(M)\cdot\overrightarrow{u^*}(M)\mathrm{d}S \tag{2}$$

where:

- $\underline{\underline{\sigma}}$ is the stress field;
- S is the surface of the studied coupon;
- S_f is the surface where the load is applied;
- $\overrightarrow{T}(M)$ are the forces per unit area (distribution of tractions) over the boundary surface S_f;
- $\overrightarrow{u^*}$ is the virtual displacement field and $\underline{\underline{\varepsilon}}^*$ the virtual strain field derived from $\overrightarrow{u^*}$.

Introducing the elastic orthotropic constitutive equations Eq. (1), and assuming that the material is homogeneous at the scale of the coupon, Eq. (2) becomes:

$$\begin{aligned} &Q_{\mathrm{RR}}D\int_S \varepsilon_{\mathrm{R}}\varepsilon_{\mathrm{R}}^*\mathrm{d}S + Q_{\Theta\Theta}D\int_S \varepsilon_\Theta\varepsilon_\Theta^*\mathrm{d}S + Q_{R\Theta}D\int_S(\varepsilon_{\mathrm{R}}\varepsilon_\Theta^* \\ &+ \varepsilon_\Theta\varepsilon_{\mathrm{R}}^*)\mathrm{d}S + Q_{\mathrm{SS}}D\int_S \varepsilon_{\mathrm{S}}\varepsilon_{\mathrm{S}}^*\mathrm{d}S = \int_{S_f}\overrightarrow{T}(M)\cdot\overrightarrow{u^*}(M)\mathrm{d}S \end{aligned} \tag{3}$$

Four independent virtual displacement fields $\{\overrightarrow{u^{*a}},\underline{\underline{\varepsilon}}^{*a}\}$, $\{\overrightarrow{u^{*b}},\underline{\underline{\varepsilon}}^{*b}\}$, $\{\overrightarrow{u^{*c}},\underline{\underline{\varepsilon}}^{*c}\}$ and $\{\overrightarrow{u^{*d}},\underline{\underline{\varepsilon}}^{*d}\}$ have to be chosen to identify Q_{RR}, $Q_{\Theta\Theta}$, $Q_{R\Theta}$ and Q_{SS} independently. They should be kinematically admissible, i.e. continuous, differentiable and consistent with the actual boundary conditions.

Thus, a system of four linear equations is obtained where Q_{RR}, $Q_{\Theta\Theta}$, $Q_{R\Theta}$ and Q_{SS} are the four unknowns:

$$\mathbf{A}\times\mathbf{Q} = \mathbf{B} \tag{4}$$

$\mathbf{A}$ is a 4×4 square matrix that represents the contribution of the internal virtual work and $\mathbf{B}$ is a 4×1 matrix that represents the external virtual work divided by the thickness D. The unknown vector $\mathbf{Q}$ is determined by inverting the system of equations.

One of the critical points of the method is the choice of the four virtual fields $\{\overrightarrow{u^{*a}},\underline{\underline{\varepsilon}}^{*a}\}$, $\{\overrightarrow{u^{*b}},\underline{\underline{\varepsilon}}^{*b}\}$, $\{\overrightarrow{u^{*c}},\underline{\underline{\varepsilon}}^{*c}\}$ et $\{\overrightarrow{u^{*d}},\underline{\underline{\varepsilon}}^{*d}\}$ that must lead to four independent equations. It has been shown [16] that some virtual fields called special virtual fields render $\mathbf{A}$ equal to unity. Eq. (4) leads therefore to the direct identification of the unknown parameters because three out of the four terms of each row are equal to zero, whereas the fourth one in the diagonal is equal to 1 (the dimension is $m2$ for ensuring dimensional homogeneity).

Finally, the solution is:

$$\begin{aligned} Q_{\mathrm{RR}} &= \frac{1}{D}\int_{S_f}\overrightarrow{T}.\overrightarrow{u^{*a}}\,\mathrm{d}S \qquad Q_{\Theta\Theta} = \frac{1}{D}\int_{S_f}\overrightarrow{T}.\overrightarrow{u^{*b}}\,\mathrm{d}S \\ Q_{R\Theta} &= \frac{1}{D}\int_{S_f}\overrightarrow{T}.\overrightarrow{u^{*c}}\,\mathrm{d}S \qquad Q_{\mathrm{SS}} = \frac{1}{D}\int_{S_f}\overrightarrow{T}.\overrightarrow{u^{*d}}\,\mathrm{d}S \end{aligned} \tag{5}$$

2.3. Choice of virtual fields

In practice, if the basis of functions used to select the virtual fields is sufficiently broad, a great number of special virtual fields leading to Eq. (5) can be found. A method for selecting one of these special virtual fields has recently been developed [16]. It relies on the minimization of the effect of noise on the identified parameters. Only the main features of this method will be recalled here.

The measured cartesian strains (the optical method will provide the strains in the cartesian coordinate system) ε_x, ε_y and ε_s will contain noise. The model assumed here for the noise is a Gaussian white noise. Although the present authors are well aware that this assumption is too simplistic, it is still thought that it could be a helpful criterion to select good virtual fields among the many available special fields. So this noise, respectively γN_x, γN_y and γN_s, adds to ε_x, ε_y and ε_s. γ is a strictly positive real number that represents the random variability of the strain measurements (it is interpreted as the uncertainty of the strain measurements). The noise is assumed to be uncorrelated from one measurement location to another in the current model. The components are also assumed to be uncorrelated between each other. Again, since experimentally, the strains will be derived from the two in-plane displacement components bearing the noise, this is not strictly true but this assumption is needed to keep the process analytical.

Computing ε_R, ε_Θ and ε_S in polar coordinates from ε_x, ε_y and ε_s leads to noisy values because the measured strains in cartesian coordinates are noisy.

A standard Gaussian noise, respectively γN_R, γN_Θ and γN_S, adds to ε_R, ε_Θ and ε_S.

N_R, N_Θ and N_S are linked to N_x, N_y and N_s by the coordinate rotation matrix:

$$\begin{pmatrix} N_R \\ N_\Theta \\ N_S \end{pmatrix} = \underbrace{\begin{bmatrix} \cos^2\theta & \sin^2\theta & \sin\theta\cos\theta \\ \sin^2\theta & \cos^2\theta & -\sin\theta\cos\theta \\ -2\sin\theta\cos\theta & 2\sin\theta\cos\theta & \cos^2\theta-\sin^2\theta \end{bmatrix}}_{P} \begin{pmatrix} N_x \\ N_y \\ N_s \end{pmatrix} \tag{6}$$

According to this linear equation, and unlike N_x, N_y and N_s, N_R, N_Θ and N_S are not statistically independent: they are correlated between each other. The inter correlation is

characterized by the covariance matrix of N_R, N_Θ and N_S: $M_{\text{cov}} = P \times P^T$.

As ε_R, ε_Θ and ε_S are random, the value of each unknown parameter identified from ε_R, ε_Θ and ε_S with Eq. (5) is a random variable. For example, Q_{RR} is given by:

$$\begin{aligned} Q_{\text{RR}} = & \frac{1}{D}\int_{S_f} \overrightarrow{T}\cdot\overrightarrow{u^{*a}}\,\mathrm{d}A + \gamma\left[Q_{\text{RR}}\int_S N_R\varepsilon_R^{*a}\mathrm{d}S\right. \\ & + Q_{\Theta\Theta}\int_S N_\Theta\varepsilon_\Theta^{*a}dS + Q_{\text{SS}}\int_S N_S\varepsilon_S^{*a}\mathrm{d}S + Q_{R\Theta}\int_S [N_R\varepsilon_\Theta^{*a} \\ & \left. + N_\Theta\varepsilon_R^{*a}]\mathrm{d}S\right] \end{aligned} \tag{7}$$

$Q_{\Theta\Theta}$, $Q_{R\Theta}$ and Q_{SS} are also random variables. According to Eq. (7), it can be shown that the variances of Q_{RR}, $Q_{\Theta\Theta}$, $Q_{R\Theta}$ and QSS write [16]:

$$\begin{cases} V(Q_{RR}) = (\eta^a)^2\gamma^2 \\ V(Q_{\Theta\Theta}) = (\eta^b)^2\gamma^2 \\ V(Q_{R\Theta}) = (\eta^c)^2\gamma^2 \\ V(Q_{SS}) = (\eta^d)^2\gamma^2 \end{cases} \tag{8}$$

where

$$\begin{aligned} (\eta^\alpha)^2 = & \left\{\int_S \left[Q_{RR}^2\cos^2\theta + Q_{R\Theta}^2\cos^2\theta\right.\right. \\ & + 2Q_{RR}Q_{R\Theta}\sin^2\theta\left](\varepsilon_R^{*\alpha})^2\mathrm{d}S + \int_S\left[Q_{\Theta\Theta}^2\cos^2\theta\right. \\ & + Q_{R\Theta}^2\cos^2\theta + 2Q_{\Theta\Theta}Q_{R\Theta}\sin^2\theta\left](\varepsilon_\Theta^{*\alpha})^2\mathrm{d}S\right. \\ & + \int_S\left[Q_{SS}^2(\cos^2\theta - \sin^2\theta)\right](\varepsilon_S^{*\alpha})^2\mathrm{d}S + 2\int_S\left[(Q_{R\Theta}^2\right. \\ & + Q_{RR}Q_{\Theta\Theta})\sin^2\theta + Q_{RR}Q_{R\Theta}\cos^2\theta \\ & + Q_{\Theta\Theta}Q_{R\Theta}\cos^2\theta\left](\varepsilon_R^{*\alpha}\varepsilon_\Theta^{*\alpha})\mathrm{d}S\right. \\ & + 2\int_S\left[-2Q_{RR}Q_{SS}\sin\theta\cos\theta\right. \\ & \left. + Q_{R\Theta}Q_{SS}\sin^2\theta\right](\varepsilon_R^{*\alpha}\varepsilon_S^{*\alpha})\mathrm{d}S + 2\int_S\left[Q_{\Theta\Theta}Q_{SS}\sin^2\theta\right. \\ & \left.\left. -2Q_{R\Theta}Q_{\text{SS}}\sin\theta\cos\theta\right](\varepsilon_\Theta^{*\alpha}\varepsilon_S^{*\alpha})\mathrm{d}S\right\}S \\ & \text{for}\quad \alpha = a, b, c, \text{ and } d. \end{aligned} \tag{9}$$

Therefore, computing η^α quantifies the sensitivity to noise of the method. For a given virtual field, the lowest η^α, the most accurate the identification. It has been shown [16] that, for given strain fields $\underline{\varepsilon_R}$, ε_Θ and $\underline{\varepsilon_S}$, there is a unique set of special virtual fields $\{\overrightarrow{u^{*a}}, \underline{\underline{\varepsilon^{*a}}}\}$, $\{\overrightarrow{u^{*b}}, \underline{\underline{\varepsilon^{*b}}}\}$, $\{\overrightarrow{u^{*c}}, \underline{\underline{\varepsilon^{*c}}}\}$ and $\{\overrightarrow{u^{*d}}, \underline{\underline{\varepsilon^{*d}}}\}$ which minimize respectively the sensitivity to noise η^α, for $\alpha = a$, b, c, or d. These four virtual fields are deduced from the resolution of a constrained minimization problem. The unknowns of this minimization problem are the components of the virtual fields expanded in a suitable basis of continuous functions. The Lagrangian of the problem is written. Its unique saddle point is found [16], yielding the virtual field that is the less sensitive to noise for each unknown constitutive parameter. However, the problem is not explicit because the unknowns Q_{RR}, $Q_{\Theta\Theta}$, $Q_{R\Theta}$ and Q_{SS} are involved in the expression of η^α. The problem is solved by an iterative algorithm where the unknown parameters are replaced by their identified value. A first set of initial values is chosen. Tests showed that this algorithm converges in less than 4 iterations whatever the choice of the initial values [16].

Finally, each unknown constitutive parameter can be identified by applying the VFM with these optimized special virtual fields.

2.4. Choice of a region of interest

In order to optimize the spatial resolution of the full-field measurements, only a reduced part of the ring surface is investigated. Indeed, if all the ring lateral surface is studied, only 26% of the pixels of the camera are located onto the ring surface, the remaining pixels being either inside the ring, or outside. However, if only a 30° angular sector of the ring is studied, more than 50% of the pixels of the camera are located onto the ring surface and the spatial resolution is therefore significantly improved.

The choice of the active zone is based on simulated data. The mechanical response of the ring subjected to diametral compression is computed with the finite element ANSYS software. The applied load is $F = 20{,}000$ N. An orthotropic linear elastic behaviour law is considered, with the following parameters: $E_{RR} = 10$ GPa, $E_{\Theta\Theta} = 40$ GPa, $\nu_{\Theta R} = 0.3$

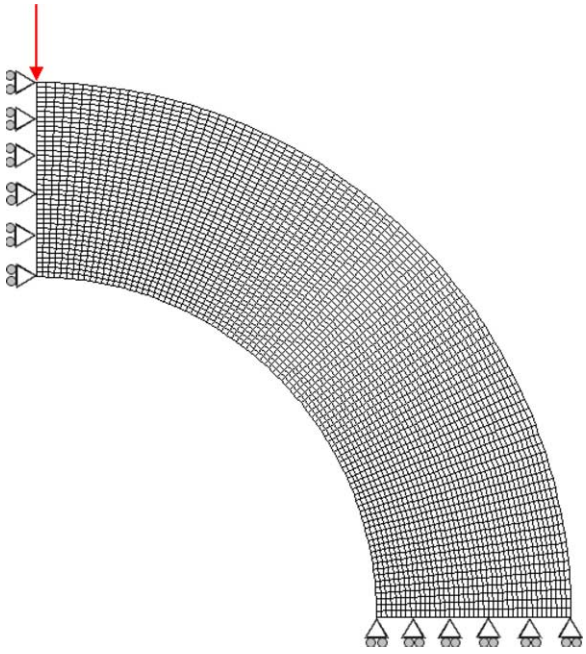

Fig. 2. Finite element model mesh.

Table 1
Sensibility to noisy data for several zones of study

	0–30°	10–40°	20–50°	30–60°	40–70°	50–80°	60–90°
$\eta(Q_{RR})/Q_{RR}$	196	210	261	382	281	174	76
$\eta(Q_{\Theta\Theta})/Q_{\Theta\Theta}$	118	107	99	105	106	100	74
$\eta(Q_{R\Theta})/Q_{R\Theta}$	211	234	302	477	545	302	138
$\eta(Q_{SS})/Q_{SS}$	90	86	77	61	45	33	21
$(\eta/Q)_{\text{average}}$	154	159	185	256	244	152	77

and $G_{R\Theta}=4$ GPa. A regular mesh of 3600 bilinear elements is defined over a quarter of the ring (Fig. 2). The locations (X_k, Y_l) where strain data are simulated, with $1<k<p$ and $1<l<q$, correspond to the centroids of the elements. These data are then input into the VFM procedure described previously and the coefficients of sensitivity to noise η^{α}, for $\alpha=a$, b, c or d can be computed for the regions of interest varying from 0–30° to 60–90° by increments of 10°.

The zone that presents the lowest noise sensitivity average is the 60–90° one (Table 1). However, this zone is just under the loading point. The plane stress assumption can be affected in this zone because of Saint-Venant effects [5,6]. Moreover, this area will see high strain concentrations and the spatial resolution of the optical technique will not be sufficient to measure these correctly. Therefore, the zones near the loading point have been discarded.

Among the remaining zones, the best one is the 0–30° (Table 1). Consequently, the study focuses on this zone in the following sections.

3. Full-field measurements with the grid method

Displacement fields have been measured using an optical method called the grid method [14,15]. A grid pattern is deposited onto the surface of the specimen. It is considered as a spatial carrier to characterize the displacement field of the specimen. The basic rules leading to the measurement of the displacement fields with this method are recalled in this section.

3.1. Printing of the grid

The spatial carrier is made up of a set of horizontal and vertical contrasted lines, with a natural spatial frequency $f_0=2.083$ line per mm. Practically, these are obtained from a professional printer through an EPS file. The prints consist of a polymer base and a photosensitive coating of very small thickness that bears the optical contrast. In order to avoid the presence of the thick polymer base at the surface of the specimen, the procedure adopted consists in bonding the film onto the specimen and then, peeling off the base. A white glue is used to ensure good final contrast. The full procedure can be found in [17].

3.2. Characterization of displacements by phase modulation

A given point M_0 of the space determined by its position vector $\overrightarrow{R}(X,Y)$ in the reference cartesian frame $(O, \overrightarrow{i}, \overrightarrow{j})$ is considered. In the initial undeformed configuration, material point M coincides with M_0. In the final deformed configuration, another material point M' coincides with the spatial point M_0. The position of M' in the initial undeformed configuration was characterized by $\overrightarrow{R}'(X',Y')$ in the cartesian reference frame.

In the initial undeformed state, the reflected light at point M_0 is the light reflected by material point M. Its intensity writes:

$$I(\overrightarrow{R}) = I_0\{1 + \gamma \text{frng}[2\pi \overrightarrow{F}\cdot\overrightarrow{R}]\} \tag{10}$$

where:

- I_0 is the local intensity bias,
- γ is the contrast,
- frng is a 2π-periodic continuous function,
- $\overrightarrow{u}.\overrightarrow{v}$ denotes the dot product of both vectors $\overrightarrow{u}(u_x,u_y)$ and $\overrightarrow{v}(v_x,v_y)$:

$$\overrightarrow{u}\cdot\overrightarrow{v} = u_x v_x + u_y v_y \tag{11}$$

- $\overrightarrow{F}$ is the spatial frequency vector. It is orthogonal to the grid lines and its amplitude is the spatial frequency of the grid. If the grid lines are vertical, they are parallel to $\overrightarrow{j}$, meaning that the spatial frequency vector writes $\overrightarrow{F}(f_0,0)$. If the grid lines are horizontal, they are parallel to $\overrightarrow{\imath}$, meaning that the spatial frequency vector writes $\overrightarrow{F}(0,f_0)$.

When a loading is applied, there is a deformation of the structure and the grid is also deformed. The reflected light at spatial point M_0 has become the light reflected by the material point M'. As the position of M' in the undeformed configuration is determined by $\overrightarrow{R}'(X,Y)$, the new intensity at point M_0 is actually:

$$I(\overrightarrow{R}) = I_0\{1 + \gamma\ \text{frng}[2\pi \overrightarrow{F}\cdot\overrightarrow{R}']\} \tag{12}$$

The deformation from the undeformed configuration to the deformed configuration is described mathematically by the displacement field $\overrightarrow{U}(\overrightarrow{R}')=\overrightarrow{R}-\overrightarrow{R}'$, but also by the inverse displacement field $\overrightarrow{U}^{-1}(\overrightarrow{R})=\overrightarrow{R}-\overrightarrow{R}'$. Therefore Eq. (12) writes:

$$I(\vec{R}) = I_0\{1 + \gamma\ \mathrm{frng}[2\pi\vec{F}\cdot(\vec{R} - \vec{U}^{-1}(\vec{R}))]\} \quad (13)$$

The phase of the function frng at point M varies of $2\pi\vec{F}.\vec{U}^{-1}(\vec{R})$ from the undeformed to the deformed state. If the assumption of small deformations is valid, $\vec{U}^{-1}(\vec{R})$ and $\vec{U}(\vec{R})$ are similar. Therefore, it can be written in the deformed state:

$$I(\vec{R}) = I_0\{1 + \gamma\ \mathrm{frng}[2\pi\vec{F}\cdot(\vec{R} - \vec{U}(\vec{R}))]\} \quad (14)$$

The first component $U_x(x, y)$ of the displacement is calculated from the phase of the function frng when the grid lines are vertical, the second component $U_y(x, y)$ when the grid lines are horizontal. The phase fields are computed by using the spatial phase shifting method implemented in a Matlab routine [18,19].

3.3. Measurement of displacement fields

The $U_x(x, y)$ and $U_y(x, y)$ displacement components relative to the unloaded configuration are calculated from the respective phase differences $\Delta\phi_X$ (for vertical lines) and $\Delta\phi_Y$ (for horizontal lines) introduced by the deformation:

$$U_x(x, y) = -\frac{p}{2\pi}\Delta\phi_X(x, y) \quad (15)$$

$$U_y(x, y) = -\frac{p}{2\pi}\Delta\phi_Y(x, y) \quad (16)$$

where $p = 0.48$ mm here. The resolution of the method, i.e. the smallest displacement which can be measured in absolute value, depends on the measurement noise. The noise is a random variable which adds to the phase during the calculation [18]. Its mean is 0 and its standard deviation is denoted σ_ϕ. In our experiments, σ_ϕ lies between $2\pi/360$ and $2\pi/240$, meaning that the resolution of the method for measuring displacements lies between 1.4 and 2.1μm.

3.4. Strain field computation

To compute the strain field components, displacement fields must be differentiated according to:

$$\varepsilon_{ij} = \frac{1}{2}\left[\frac{\partial u_i}{\partial x_j} + \frac{\partial u_j}{\partial x_i}\right]; \quad i, j \in [1 - 3] \quad (17)$$

Several methods are available in the literature for numerically differentiating displacement fields:

- point-wise [20]

$$\varepsilon(x) = \frac{u(x + \Delta x) - u(x)}{\Delta x} \quad (18)$$

- by fitting a plane to $P \times P$ pixels subimages of the displacement fields [15,21]. Then, the gradient of the plane along the relevant axis provides an estimate of the strain component at the central pixel of the subimage.
- by projecting the whole displacement field onto a basis of generic functions [22,23] which can be differentiated analytically.

Table 2
Influence of the polynomial fitting on the identification

	E_{RR} (GPa)	$E_{\Theta\Theta}$ (GPa)	$\nu_{\Theta R}$ (*no dim.*)	$G_{R\Theta}$ (GPa)
Strains assessed with the FEM shape functions	9.64	39.3	0.309	4.05
Strains assessed by differentiating FEM displacement fields point-wise	9.75	41.3	0.289	3.80
Strains assessed by differentiating FEM displacement fields with a polynomial fit	9.29	40.7	0.292	3.83
Strains assessed by differentiating FEM displacement fields + modelled noise with a polynomial fit	9.17	40.8	0.296	3.86
Reference values	10	40	0.3	4

The solution chosen here is the third one because it is the less sensitive to noise and also because displacement fields are smooth enough in the region of interest for being fitted by polynomials of low degree. Generally speaking, this solution is very efficient when the spatial frequency ranges of the signal (strain field) and noise are well separated.

Polynomials of degree 4 are used to fit the whole displacement fields. Strain fields are derived by computing the closed form derivatives of the polynomials. The main advantage of this solution is that displacement fields can be interpolated at the locations of missing or inconsistent data.

To validate this approach, an application of this method for differentiating displacement fields has been performed on simulated finite element displacements. The Virtual Fields Method provided very similar results from strain fields obtained either by polynomial fitting or using the

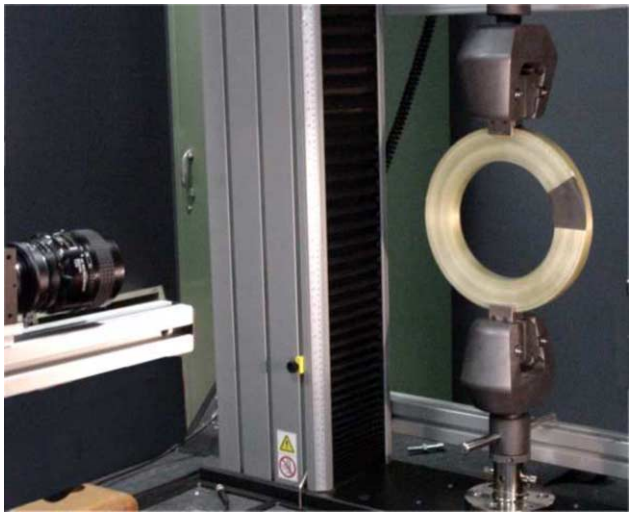

Fig. 3. Experimental set-up.

shape functions of the finite elements (Table 2). Therefore, it proves that the method chosen to compute strain fields is accurate enough for the present application.

4. Identification

4.1. Mechanical set-up with one camera

An INSTRON universal testing machine is used to perform the diametral compression test. Rubber is used at each point of application of the load to improve the contact pressure distribution and avoid compression damage of the composite in the vicinity of the load application. It also serves to prevent the specimen from slipping out of the fixture.

A grid has been bonded onto the ring which is then positioned in the fixture so that the grid lies in the chosen zone of interest (Fig. 3). The grid period is 480 μm. The lens is set such that a period of the grid is sampled by 6 pixels of the CCD camera. In these conditions, the spatial resolution is 0.96 mm and the resolution of displacement measurements is 2.3 μm.

Five tests have been carried out on the same specimen with an applied load of 20 kN. The 20 kN load limit has been chosen so as to avoid damaging of the specimen

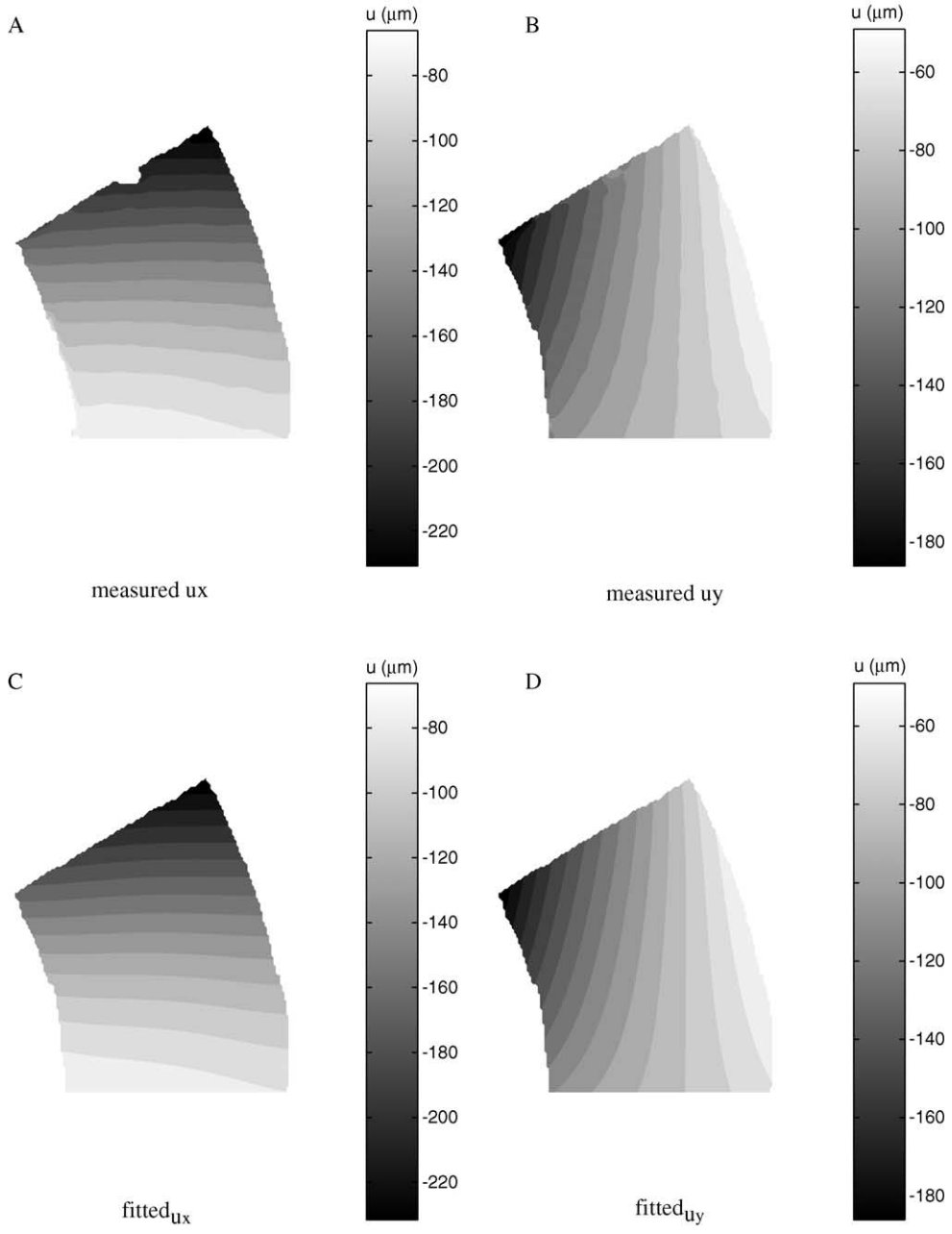

Fig. 4. Measured and fitted displacement fields ($F = 20$ kN).

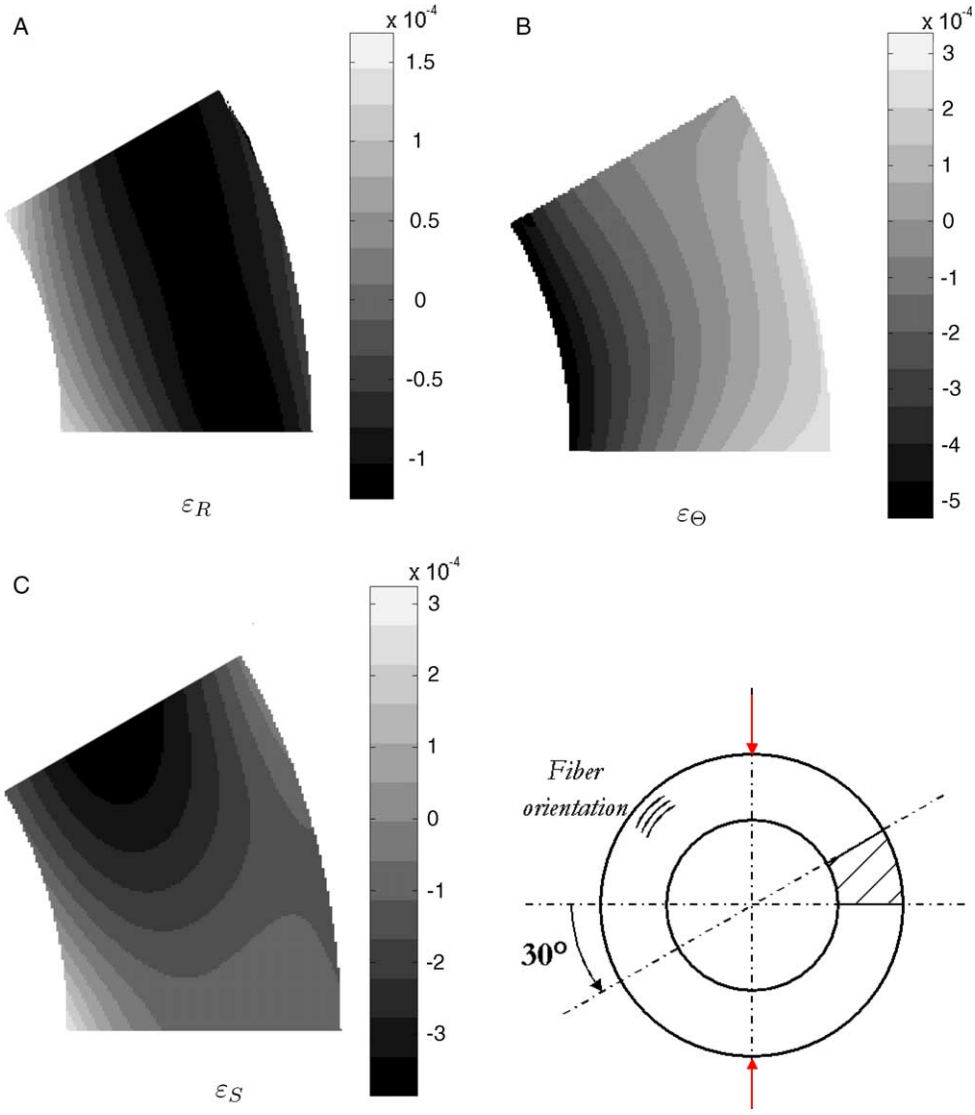

Fig. 5. Experimental strain fields ($F = 20$ kN).

because of overloading. Indeed, the maximal strain criterion has been applied to the specimen. Damage can occur in glass-epoxy for shear strains of 0.2%. Achieving FE computations, it has been shown that this criterion is reached in the region below the loading point for applied loads just over 20 kN. Accordingly, 20 kN is the best load to apply for providing the largest strains within the elastic response domain of the ring.

Only the initial and the final images of the grid are grabbed. Thus, displacement and strain fields are measured only for one load. This is sufficient here since only elastic stiffnesses are required.

4.2. Results obtained with one camera

The measured displacement fields (Fig. 4) were fitted with polynomials of degree 4 and differentiated. The strain fields thus obtained (Fig. 5) are similar to those computed with the finite element model (Fig. 6), but the values are quite different. This indicates that the actual moduli are different from those used in the finite element model.

The moduli identified from those strain fields are reported in Table 3. Their average is quite consistent with the reference values of a glass-epoxy material. However, the coefficient of variations are very high, much higher than the values computed from Eq. (9). It means that the scatter of the results is far out of the range of scatter that could be induced by noise effects. According to the sensitivity to noise computed in Eq. (9) and according to the noise level in the measurements, the coefficient of variation of the moduli should not exceed 50% in the worst case. So, there is another problem causing this.

The most restrictive assumption in the identification procedure is that the stress distribution is uniform across the thickness of the specimen. This assumption may be a bit too restrictive considering the 21.5 mm depth of the specimen. Any misalignment in the vertical positioning of the ring will

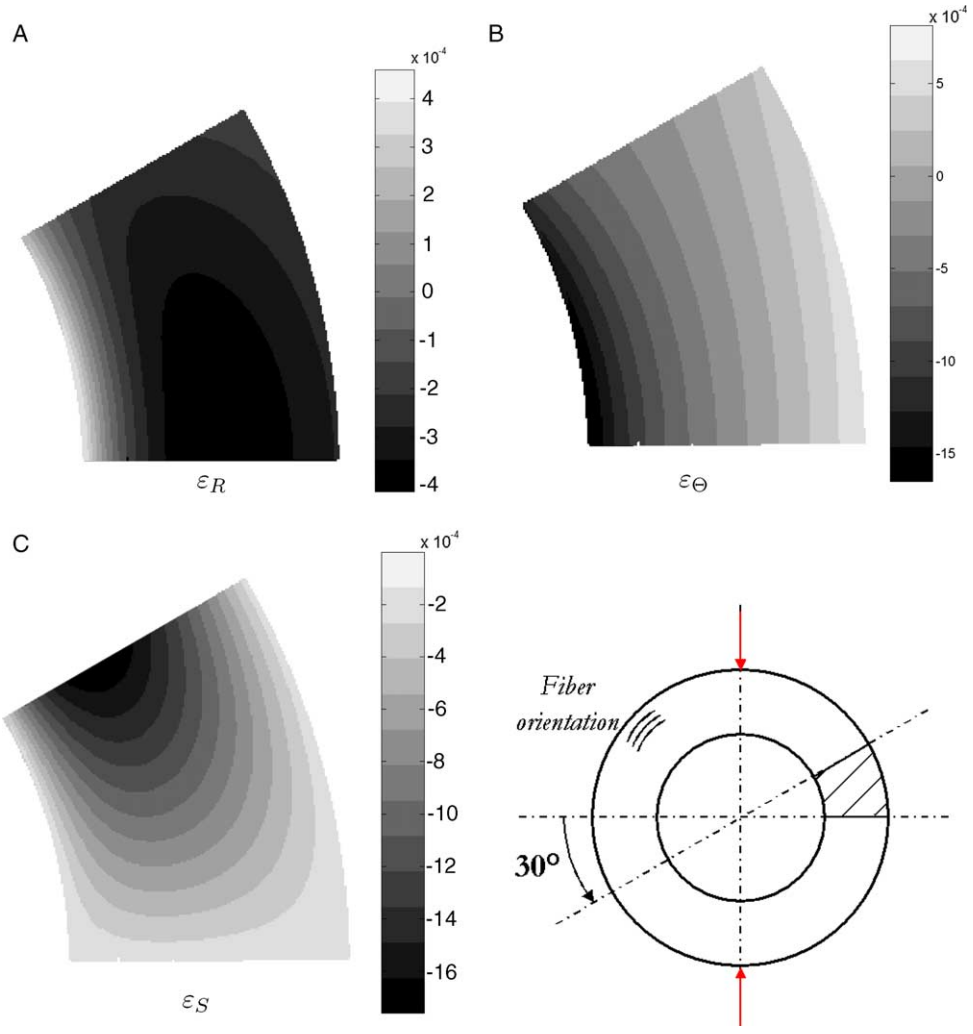

Fig. 6. Simulated strain fields ($F = 20$ kN).

cause non uniform strain and stress distribution through the thickness.

In order to check this assumption, strains have been measured locally with two sets of back-to-back strain gauges bonded at two different locations (Fig. 7). Both groups of gauges put the parasitic effect in evidence. There is a large discrepancy between the strains measured by the gauge on the front face and the strains measured by the gauge on the back face (Fig. 8). This proves that the strain distribution is far from being uniform through the depth of the ring. It must also be noted that the discrepancy evolution is non linear, whereas the material behaviour is linear for this range of strain values. It proves that the contact pressure distribution at the loading point is likely to

Table 3
Identified rigidities using only one camera

	Q_{RR} (GPa)	$Q_{\Theta\Theta}$ (GPa)	$Q_{R\Theta}$ (GPa)	Q_{SS} (GPa)
Test no 1	3.24	33.2	1.72	6.04
Test no 2	1.20	31.8	2.40	3.17
Test no 3	14.2	27.3	3.8	2.94
Test no 4	12.5	33.2	3.88	7.51
Test no 5	25.9	96.6	7.57	14.4
Average	11.4	44.4	3.87	6.8
Coeff. of variation	87%	66%	59%	69%
Reference for glass epoxy	10.27	40.92	3.07	4

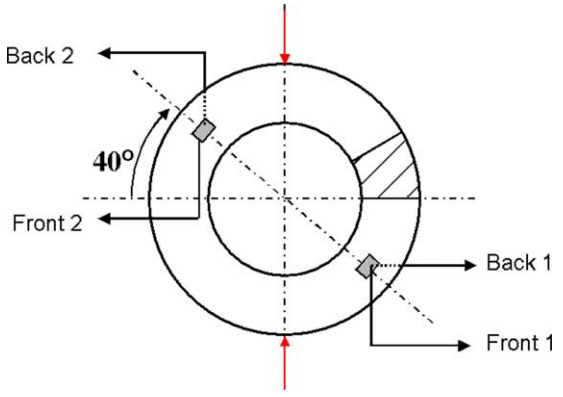

Fig. 7. Experimental set-up for monitoring strains on both side of the ring coupon.

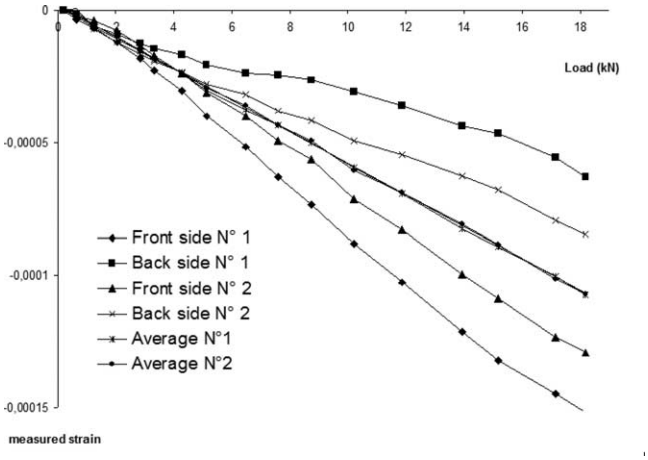

Fig. 8. Strains measured on both sides of the ring coupons with strain gauges ($\in_{\Theta}$).

be at the origin of the discrepancy, because the contact phenomenon, associated with the compression behaviour of rubber, is typically non linear. The contact distribution is also non repeatable from one test to another because it is not possible to put the ring exactly in the same position from one test to another. Therefore, the strain values from one test to another can vary even if the distribution remains similar. This can explain the high coefficients of variation of the identified stiffness even if the measured strain fields are similar to the simulated ones.

However, it is interesting to note that averaging the back to back gauge readings provides the same response at the two locations, which is what was expected. This is consistent with similar observations on other tests when testing thick composites [24,25]. In order to get rid of this effects, it was decided to measure the displacement fields on both faces of the ring using two cameras mounted back-to-back.

4.3. Results obtained with the improved mechanical set-up

Following the above idea, a new experimental set-up has been used for validating this improved approach. Two cameras and two grids are used for measuring simultaneously the displacement fields on both sides of the ring coupon (Fig. 9). The new procedure consists in:

- measuring the displacement fields on both sides of the specimen,
- deducing the actual in-plane displacement field as the average value of both side displacements,
- differentiating the average displacement field to get the actual in-plane strain,
- and identifying the stiffness values from the derived in-plane strain.

Nine tests have been carried out on the same specimen with an applied load of 20 kN using the improved set-up. The procedure is exactly the same as previously.

The identified stiffnesses are reported in Table 4. Their average is still consistent with the reference values of a glass-epoxy material. One can be surprised by the high value of Q_{SS}. Values closer to 4 GPa would have been expected for a glass epoxy unidirectional laminate. This cannot come from a problem in the identification programme since it has been successfully validated with simulated data. However, it is very difficult to obtain reference values in this case, which is the very reason why the present approach has been used. Nevertheless, on the whole, the average values are fairly satisfactory. Moreover, the coefficients of variations have strongly improved compared to the first results. Their order is consistent with the theoretical noise sensitivity factors computed from Eq. (9) and given in Table 1 for the 0–30°. zone, proving the relevancy of the noise effect minimization. The coefficients of variation remain higher than 20% for Q_{RR} and $Q_{R\Theta}$ but they are identified using only one loading at 20 kN. An accurate value of the moduli can be obtained in practice by loading the ring step by step from 0 N up to 20 kN as it is usually adopted to characterize the stress/strain curve of materials with standard tests.

5. Summary

In this paper, a novel experimental procedure has been successfully demonstrated for providing all the through-thickness rigidities of a thick filament-wound glass-epoxy composite tube. The procedure requires diametral

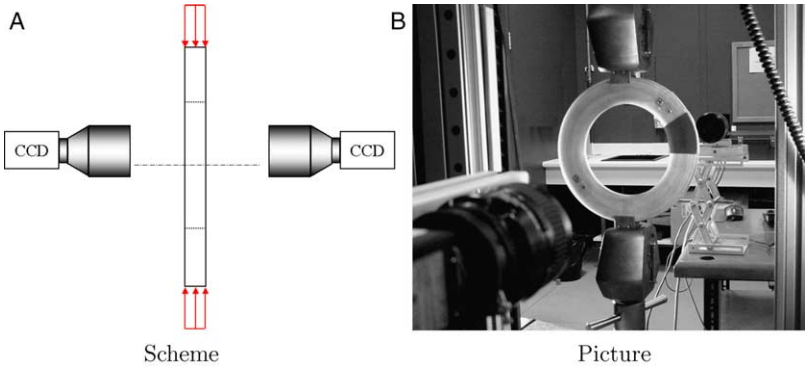

Fig. 9. Optical system providing directly the images of both sides of the specimen.

Table 4
Identified rigidities using the improved set-up with two cameras

	Q_{RR} (GPa)	$Q_{\Theta\Theta}$ (GPa)	$Q_{R\Theta}$ (GPa)	Q_{SS} (GPa)
Test no 1	13.1	48.3	3.08	6.77
Test no 2	12.6	45.4	2.04	6.93
Test no 3	15.7	46	2.26	6.88
Test no 4	13.3	44.6	1.92	6.36
Test no 5	9.46	49.4	3.8	6.96
Test no 6	10.9	47.2	3.86	6.41
Test no 7	10.1	45.9	2.44	7.1
Test no 8	8.44	39.6	2.2	6.54
Test no 9	8.95	41.9	2.03	7.12
Average	11.4	45.4	2.62	6.78
Coeff. of variation	29%	10%	29%	4%
Engineering constants:	E_{RR}	$E_{\Theta\Theta}$	$\nu_{\Theta R}$	$G_{R\Theta}$
	11.3 GPa	44.8 GPa	0.23	6.78 GPa

compression tests to be performed on ring coupons cut from the tubes, then to measure the strain fields over the lateral surface of a loaded ring, and finally to process the strain fields with the Virtual Fields Method.

Experimentation proved that the procedure yields consistent and repeatable values of the four unknown orthotropic rigidities provided that the average of the displacement fields measured over both sides of the specimen is processed instead of the fields measured only over one side. Moreover, the scatter obtained can indeed be related to the theoretical coefficients of variations provided by the VFM, validating the approach of special optimized virtual fields from an experimental point of view.

It is the first time that such consistent data have been obtained experimentally using the VFM, showing that the procedure is now ready for industrial transfer. The potential of such inverse identification from heterogeneous fields and full-field strain measurements is tremendous and may well lead to a very significant update of material testing procedures in the future.

Acknowledgements

The present authors would like to thank Dr Peter Davies from Ifremer Brest (France) for providing the ring coupons.

References

[1] Broughton WR, Sims GD. An overview of through-thickness test methods for polymer matrix composites. Technical report, DMMA(A) 148. UK: Natinal Physics Laboratory; 1994.
[2] Mespoulet S. Through-thickness test methods for laminated composite materials. PhD thesis, Imperial College of Science, Technology and Medecine; 1998.
[3] Gipple KL, Hoyns D. Measurement of the out-of-plane shear response of thick section composite materials using the V-notched beam specimen. J Compos Mater 1994;28:543–72.
[4] Hiel C, Surnish M, Chappell D. A curved beam specimen for determining the interlaminar tensile strength of a laminated composite. J Compos Mater 1994;25:543–72.
[5] Arimitsu Y, Nishioka K, Senda T. A study of Saint Venant's principle for composite materials by means of internal stress fields. J Appl Mech 1995;62:53–62.
[6] Pierron F, Alloba E, Surrel Y, Vautrin A. Whole-field assessment of the effects of boundary conditions on the strain field in off-axis tensile testing of unidirectional composites. Compos Sci Technol 1998; 58(12):1939–47.
[7] Grédiac M. Principe des travaux virtuels et identification. Mécanique des Solides 1989;309(II):1–5 [Comptes rendus de l'Académie des Sciences, in french with an English abstract].
[8] Grédiac M. The use of heterogeneous strain fields for the characterization of composite materials. Compos Sci Technol 1996; 56:841–6 [Elsevier].
[9] Grédiac M, Pierron F, Surrel Y. Novel procedure for complete in-plane composite characterization using a T-shaped specimen. Exp Mech 1999;39(2):142–9 [Society for Experimental Mechanics].
[10] Grédiac M, Fournier N, Paris P-A, Surrel Y. Direct measurement of invariant parameters of composite plates. J Compos Mater 1999; 33(20):1939–65 [Pergamon].
[11] Pierron F, Zhavoronok S, Grédiac M. Identification of through-thickness properties of thick laminated tubes using the virtual fields method. Int J Solids Struct 2000;37(32):4437–53.
[12] Pierron F, Grédiac M. Identification of the through-thickness moduli of thick laminates from whole-field measurements using the Iosipescu fixture: theory and simulations. Composites Part A 2000;31(4): 309–18 [Elsevier].
[13] Hendriks MAN. Identification of the mechanical properties of solid materials. Doctoral dissertation, Eindhoven University of Technology; 1991.
[14] Surrel Y. Moiré and grid methods: a signal-processing approach. In: Pryputniewicz RJ, Stupnicki J, editors. Interferometry'94: photomechanics, vol. SPIE 2342.
[15] Avril S, Ferrier E, Hamelin P, Surrel Y, Vautrin A. A full-field optical method for the experimental analysis of reinforced concrete beams repaired with composites. Composite Part A 2004;35(7):873–84 [Elsevier].
[16] Avril S, Grédiac M, Pierron F. Sensitivity of the virtual fields method to noisy data. Comput Mech 2004;34(6):439–52 [Springer].
[17] Piro J-L, Grédiac M. Producing and transferring low-spatial-frequency grids for measuring displacement fields with moiré and grid methods. Exp Tech 2004;28(4):23–6.
[18] Surrel Y. Fringe analysis. In: Rastogi PK, editor. Photomechanics. Berlin: Springer; 1999. p. 57–104.
[19] Surrel Y. Design of algorithms for phase measurements by the use of phase-stepping. Appl Opt 1996;35:60–1.
[20] Périé J-N, Calloch S, Cluzel C, Hild F. Analysis of a multiaxial test on a C/C composite by using digital image correlation and a damage model. Exp Mech 2004;42(3):318–28.
[21] Kajberg J, Lindkvist G. Characterisation of materials subjected to large strains by inverse modelling based on in-plane displacement fields. Int J Solids Struct 2004;41:3439–59 [Elsevier].
[22] Roux S, Hild F, Berthaud Y. Correlation image velocimetry: a spectral approach. Appl Opt 2002;41(1):108–15.
[23] Wagne B, Roux S, Hild F. Spectral approach to displacement evaluation from image analysis. Eur Phys J AP 2002;17:247–52.
[24] Pierron F. Saint-Venant effects in the Iosipescu specimen. J Compos Mater 1998;32(22):1986–2015.
[25] Pierron F, Cerisier F, Grédiac M. A numerical and experimental study of woven composite pin-joints. J Compos Mater 1999;34(12): 1028–54.